

RESEARCH ARTICLE

Open Access



Nonlocal interaction enhanced biexciton emission in large CsPbBr₃ nanocrystals

Peng Huang¹, Shipei Sun¹, Hairui Lei³, Yongyou Zhang^{2*}, Haiyan Qin^{3*} and Haizheng Zhong^{1*}

Abstract

Biexciton emission in quantum dots is an efficient way to generate entangled photon pairs, which are key resources in quantum informatics. Compared with epitaxial grown quantum dots, chemically synthesized colloidal quantum dots show advantages of tunable wavelength and easy integration to realize quantum light sources. However, biexciton efficiency of colloidal quantum dots has been limited by Auger recombination. In this paper, we reported nonlocal interaction enhanced biexciton emission with efficiency up to 80% in large perovskite nanocrystals (> 20 nm). The nonlocal interaction between carriers and excitons leads to the abnormal exponential decrease of Auger recombination with volume in large nanocrystals, which distinguishes with the linear scaling in small counterparts. Such an exponential decrease of Auger recombination results in long lifetime of biexcitons, responsible for the required high biexciton efficiency. The discovery of nonlocal effects in large semiconductor nanocrystals provides new strategies to achieve high efficiency multiple excitons for quantum optics and energy conversation applications.

1 Introduction

Due to the size-dependent quantum confinement effects, quantum dots (QDs) exhibit excitonic properties with tunable absorption and emission properties for modern photonics [1–5]. Efficient single photon [6–8] and entangled photons [9–11] emission, which are key resources in quantum informatics [12–15], have been successfully demonstrated by combining QDs and microcavities [6–8]. Besides epitaxial grown QDs (InGaAs, GaAs) [16], chemically synthesized colloidal QDs are also considered

as ideal quantum emitters [17–22] with advantages of high photoluminescence (PL) efficiency, tunable color, and easy integration [23, 24]. Because of the strong electron–electron coulomb repulsion in small CdSe and perovskite QDs (strong quantum confined), excellent single photon emitters were successfully demonstrated [19, 25–28]. For colloidal QDs, biexciton emission is usually generated under high excitation intensity, which suffers from serious Auger recombination [17, 29]. It has been found that the Auger recombination rate decreases linearly with volume increasing in quantum confined QDs [30, 31]. In comparison, Auger recombination in bulk materials only slightly affects the biexciton recombination due to the lower carrier density and momentum conservation [32]. It can be described by adapting the charge carrier recombination *ABC* model with a constant Auger coefficient [33]. To gain high biexciton efficiency, thick shelled CdSe/CdS nanocrystals were developed to suppress Auger recombination by reducing the wave function overlap between the electrons and holes [34–37]. Accordingly, large colloidal QDs may be suitable candidates to generate efficient biexciton emission, however, has been rarely investigated. Herein we reported that the Auger recombination rate in large perovskite

*Correspondence:

Yongyou Zhang
yyzhang@bit.edu.cn
Haiyan Qin
hattieqin@zju.edu.cn
Haizheng Zhong
hzzhong@bit.edu.cn

¹ MIIT Key Laboratory for Low-Dimensional Quantum Structure and Devices, School of Materials Science & Engineering, Beijing Institute of Technology, Beijing 100081, China

² Beijing Key Laboratory of Nanophotonics and Ultrafine Optoelectronic Systems, School of Physics, Beijing Institute of Technology, Beijing 100081, China

³ Key Laboratory of Excited-State Materials of Zhejiang Province, Department of Chemistry, Zhejiang University, Hangzhou 310027, China

nanocrystals can be exponentially decreased due to the nonlocal effects.

Nonlocal effects refer to the influence of wave spatial dispersion on the light-matter interactions [38]. The spatial wavefunction usually contains a term of $e^{ik \cdot r}$, where k is the wave vector and r is the spatial coordinate. For the nanostructure with radius of R , nonlocal effects are negligible when the phase $kR \ll 1$, while become significant when kR approaches to 1 [39, 40]. In plasmonics, nonlocal effects have been successfully demonstrated to explain optical response in metallic nanostructures [41]. For exciton recombination in QDs which emits a photon, nonlocal interactions need to be considered when the size of QDs (R) approaches to $\frac{\lambda_p}{2n\pi}$ where λ_p is the wavelength of the photon and n is the refraction index of surrounding [39]. For CsPbBr₃ QDs, $\lambda_p \sim 520\text{nm}$ and $n \sim 2$, resulting in $\frac{\lambda_p}{2n\pi} \sim 40\text{nm}$. Auger recombination can be described as energy shift from an exciton to another electron or hole, or a process in which one electron or hole absorbs an exciton to a higher energy level. Accordingly, the nonlocal effects of Auger recombination are mainly determined by wavefunction of exciton. At room temperature, the estimated spatial wavelength of an exciton in CsPbBr₃ is $\sim 14\text{ nm}$ (refer to theory part in supplementary material), enabling the possibility to observe the nonlocal interaction enhanced biexciton emission in large nanocrystals with size of $>14\text{ nm}$. Benefiting from the unique defects tolerance ability of perovskite nanocrystals [42], we here observed high biexciton efficiency in large CsPbBr₃ nanocrystals.

As schematically shown in Fig. 1, there is a linear relation between biexciton Auger recombination lifetime and volume for small nanocrystals. The maximum biexciton lifetime is $\sim 100\text{ ps}$ due to the strong Auger recombination. For bulk materials, Auger recombination is mainly related to the carrier density and band structure with a constant coefficient [32]. For example, a bulk crystal with carrier density of 10^{18} is predicted to have a biexciton lifetime of $\sim 10\text{ ns}$ [43, 44]. In the meso-scale region, the nonlocal effects are expected to alternate the biexciton lifetime with volume from linear scaling to exponential, which is observed in large CsPbBr₃ nanocrystals for the first time.

2 Results

2.1 Morphologies and optical properties of large CsPbBr₃ nanocrystals

The large CsPbBr₃ nanocrystals with spheroidal shape were fabricated by using hot-injection [45] method, and the samples with rod shape were synthesized using a modified ligand assisted reprecipitation (LARP) method [46] (see details in method). Figure 2a–c shows the high-resolution transmission electron microscopy (HRTEM) images with fast Fourier transform (FFT) patterns of three typical CsPbBr₃ nanocrystals (Spheroids 1–3), which exhibit spheroidal shape of dodecahedron. The average diameters of these spheroids are $12.9 \pm 1.1\text{ nm}$ (Spheroid 1), $17.5 \pm 1.4\text{ nm}$ (Spheroid 2), and $25.8 \pm 1.8\text{ nm}$ (Spheroid 3) and their volumes are $\sim 1100\text{ nm}^3$, $\sim 2800\text{ nm}^3$, and $\sim 9000\text{ nm}^3$, respectively.

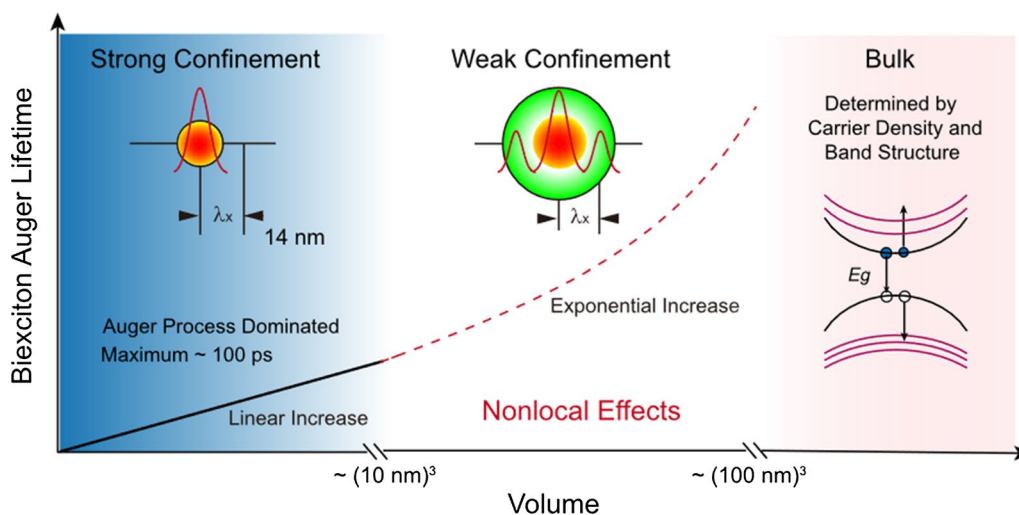


Fig. 1 The illustration of volume dependent biexciton Auger lifetime and nonlocal effects in perovskites. Auger recombination lifetime linearly increases with volume in strong confinement regime (left side), while exponentially increases in weak confinement regime (center) due to nonlocal effects. The exciton wavefunction is spatially confined in small nanocrystals, and turns to oscillation in large nanocrystals. For bulk materials, Auger recombination is mainly related to the carrier density and band structure with a constant coefficient [32]. For example, a bulk crystal with carrier density of 10^{18} is predicted to have a biexciton lifetime of $\sim 10\text{ ns}$ [43, 44]

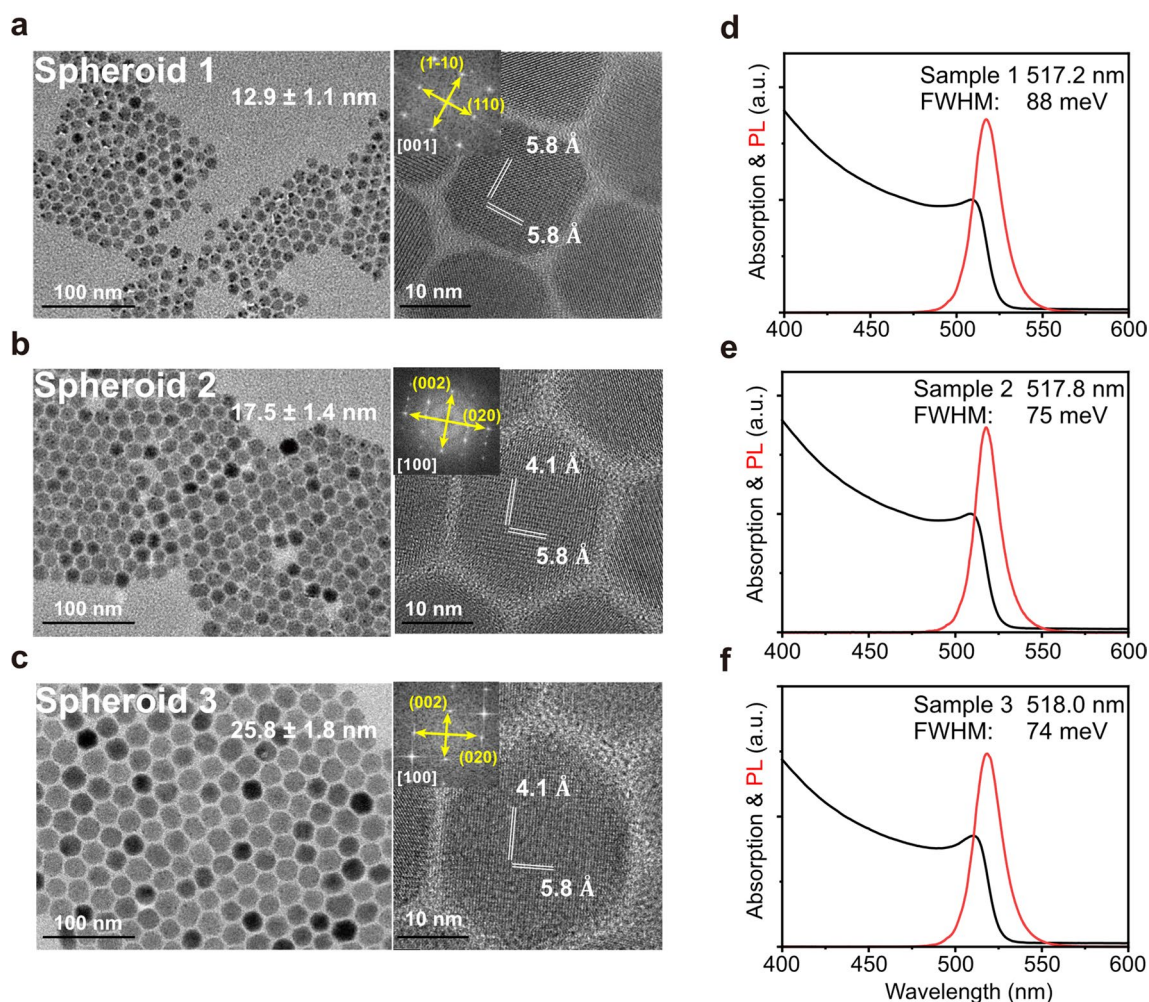


Fig. 2 Morphology, structure, and optical properties of large CsPbBr₃ nanocrystals. a-c, TEM, HRTEM images with FFT patterns of 12.9 ± 1.1 nm, 17.5 ± 1.4 nm, and 25.8 ± 1.8 nm Spheroids 1–3. d-f, The PL (red) and UV-vis absorption (black) spectra of Spheroids 1–3

Additional file 1: Fig. S1 shows the typical HRTEM and FFT images of nanorod samples (Rod 1 and Rod 2). Rod 1 has an average width of 12.0 ± 1.8 nm and an average length of $22.1 \text{ nm} \pm 3.4$ nm. Rod 2 has an average width of 13.0 ± 1.9 nm and an average length of $27.4 \text{ nm} \pm 4.8$ nm. The volumes of Rod 1 and Rod 2 are $\sim 3000 \text{ nm}^3$ and $\sim 4600 \text{ nm}^3$, respectively. As indicated by FFT patterns and powder X-ray diffractions (XRD) (see Additional file 1: Fig. S2), large CsPbBr₃ nanocrystals have an orthorhombic structure. Figure 2d–f presents the PL and UV-vis absorption spectra of Spheroids 1–3. These spheroid samples show similar PL peaks with centers around 518 nm (2.39 eV) and full width at half maximum (FWHM) of ~ 80 meV. The PL peak centers are close to the bulk bandgap of CsPbBr₃ (~ 2.36 eV at 300 K [47]), suggesting the weak quantum confinement. The PL and UV-vis absorption spectra of Rods 1–2 are shown in

Additional file 1: Fig. S3. Furthermore, these samples have high PL quantum yield (QY) (Spheroids 1–3 > 90%, Rods 1 and 2 > 70%) and good photo stability for spectroscopic measurements.

2.2 Biexciton emission of large CsPbBr₃ nanocrystals

The properties of biexcitons in nanocrystals can be measured by recording time resolved emission intensity of ensembles or single particles. Figure 3a shows an example of fluence-dependent decay traces from Spheroid 3 ensemble. As the pump power increases from $\langle N \rangle = 0.15$ to $\langle N \rangle = 2.4$ ($\langle N \rangle$ is the number of exciton pairs per particle on average), a faster PL component appears. As shown in the inset of Fig. 3b, the observed fast PL component can be assigned to the biexciton recombination due to the square relationship between its intensity and $\langle N \rangle$. Figure 3b shows a typical analysis of biexciton

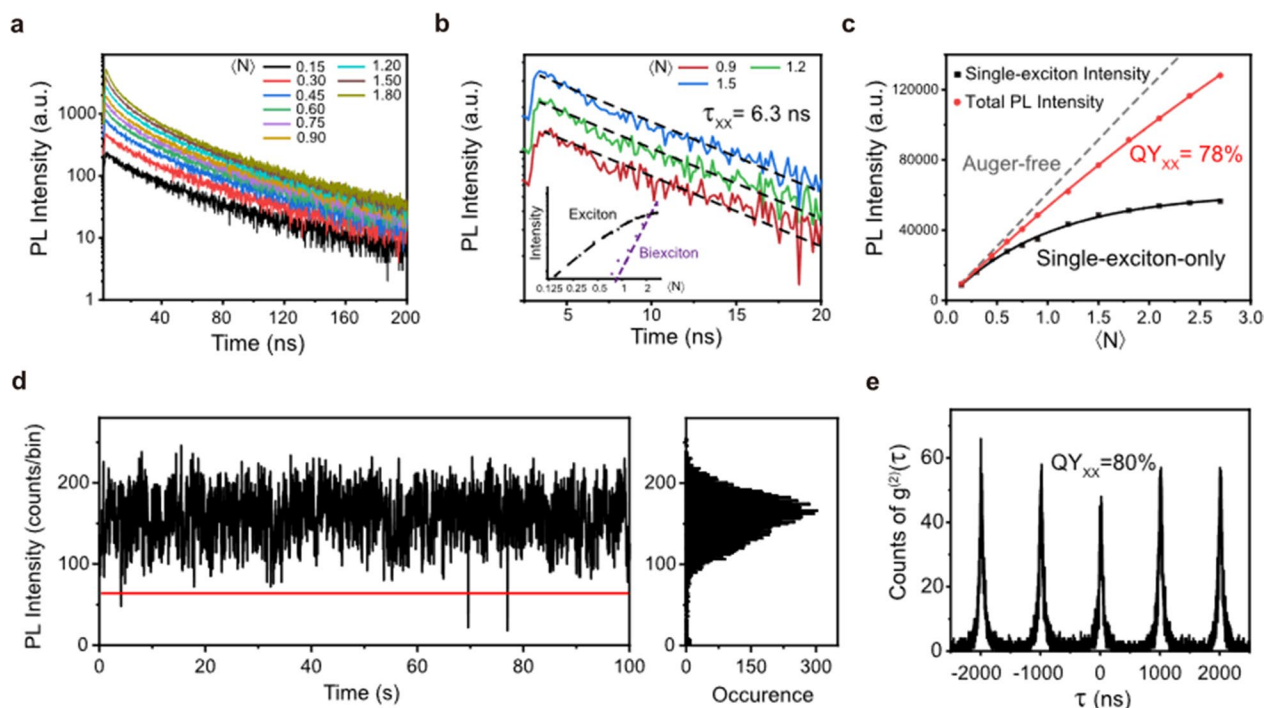


Fig. 3 Biexciton emission properties of Spheroid 3 (First row: ensemble; Second row: single particle). **a** Excitation-fluence dependent PL decay curves of a typical ensemble sample measured using a micro-liquid film method. **b** The PL recombination dynamics of biexcitons (solid lines) that extracted by subtracting the single-exciton component. They are fitted using mono-exponential decay functions (dotted lines), yielding the biexciton lifetime $\tau_{xx} \approx 6.3$ ns. The inset shows excitation-fluence dependent single-exciton (black dots) and faster component (purple dots) PL intensity extracted from (a). The excitation-fluence dependence of faster component PL intensity follows quadratic scaling (purple dotted line) of biexcitons. **c** Excitation-fluence dependent single-exciton (black dots) and total PL intensities (red dots) of ensemble sample. Solid lines are the fits to the emission saturation model for single-exciton PL (black) and total PL (red), respectively, yielding QY_{xx} of $\sim 78\%$. **d** Representative blinking traces and corresponding distribution of intensities for single particle sample. Red line was chosen as the threshold between “on” and “off” states. **e** Typical second-order photon correlation curve from single particle sample. The calculated QY_{xx} is $\sim 80\%$

lifetime of Spheroid 3 ensemble. Under the power of $\langle N \rangle = 0.15$, the PL decay curve is nearly single exponential, corresponding to the single-exciton recombination. Additional file 1: Fig. S4 shows the single-exciton recombination dynamics of these samples. The single-exciton lifetime for Spheroid 3 is ~ 35.0 ns. By subtracting the PL decay curves under the higher excitation like $\langle N \rangle = 0.9$ with that of $\langle N \rangle = 0.15$, the biexciton decay curve can be derived and fitted using single-exponential decay function. Biexciton lifetime of Spheroid 3 is ~ 6.3 ns. Figure 3c shows the excitation dependent emission intensity of single-exciton PL and total PL from Spheroid 3 ensemble. According to the fitting curves (solid lines) using standard saturation model [34], the calculated biexciton quantum yield (QY_{xx}) is $\sim 78\%$.

The biexciton properties were further investigated by applying single particle spectroscopy. Figure 3d shows the PL intensity traces of a typical single CsPbBr₃ nanocrystal from Spheroid 3 ensemble, which was measured using single-photon avalanche photodiodes (APDs) and time-tagged, time-resolved (TTTR) mode of the

time-correlated single-photon counting (TCSPC) module. The results show that Spheroid 3 is nearly nonblinking with large fraction of “On” time (PL intensity traces of other samples, see Additional file 1: Fig. S5). Figure 3e shows the second-order photon correlation curves ($g^{(2)}$) of a typical single CsPbBr₃ nanocrystal from Spheroid 3 under low excitation intensity. QY_{xx} can also be derived by calculating the area ratio between the center peak and side peak in the $g^{(2)}$ curve of single particle [48]. The results indicate that Spheroid 3 has the QY_{xx} of $\sim 80\%$. The PL dynamical behaviors of single particle were further investigated by recording the transient PL spectra under different excitation intensities. Additional file 1: Fig. S6 shows the PL intensity traces and PL decay traces at two different powers with $\langle N \rangle = 0.15$ and $\langle N \rangle = 1.2$ of single Spheroid 3. A biexciton lifetime of 7.5 ns was measured using a similar operation to subtract the contribution of single exciton recombination. By using similar measurements, we further studied the samples with different size (Spheroids 1 with 1100 nm³ and 2 with 2800 nm³) and shape (Rods 1 with 3000 nm³ and 2 with 4600 nm³). Since

the exciton quantum yield of our samples is above 90% and different scaling rule between the recombination of biexciton and that of single excitons with traps, the non-radiative recombination of single excitons can be ignored by subtracting operations [49]. The biexciton properties of these samples are shown in Additional file 1: Fig. S7–S10. The key features are summarized in Table 1, which indicates that both the biexciton efficiency and lifetime of ensemble increase with volume increasing. Their maximum values approach to ~80% and ~6.3 ns, respectively. It is also noted that the Auger recombination can be suppressed for the samples with volume over 3000 nm³.

3 Discussion

To elucidate the size dependence of biexciton emission in CsPbBr₃ nanocrystals, we extracted the reported exciton and biexciton lifetimes of perovskite nanocrystals from previous works [50–52]. Combining with our results of large perovskite nanocrystals, Fig. 4a–c plots the biexciton radiative lifetime (defined as one quarter of exciton radiative lifetime [53]), biexciton Auger recombination lifetime, and biexciton lifetime of CsPbBr₃ nanocrystals

with volume increasing. As shown in Fig. 4a, the biexciton radiative lifetime of CsPbBr₃ nanocrystals slightly varies with volume less than ~1000 nm³. When the volume exceeds ~1000 nm³, the radiative lifetime increases in power law [50]. In comparison, the biexciton lifetime shows linear scaling with volume in the small volume range, but transits to nonlinear when the volume exceeds ~1000 nm³ (Fig. 4c). To understand the nonlinear increase of biexciton lifetime in large nanocrystals, we further analyze the variation of Auger lifetime with volume in CsPbBr₃ nanocrystals. As shown in Fig. 4b, Auger recombination lifetime linearly increases in small volume range (<1000 nm³) but turns to an exponential increase in large volume range. These experimental results are consistent with the nonlocal model described in Fig. 1, confirming the significance of nonlocal effects of large nanocrystals.

The biexciton radiative lifetime can be modeled by $\tau_X = \tau_{X0} + aV^\alpha$ (τ_{X0} , a , and α are fitting parameters [50]), where τ_X and the particle volume V take the units of ps and nm³. As shown in Fig. 4a, the fitting curve (solid line) of biexciton radiative lifetime ($\tau_{r,XX}$) is in good

Table 1 The biexciton features of CsPbBr₃ nanocrystals including quantum yields, lifetime, and Auger lifetime

Sample	Volume	QY _{xx}	Biexciton lifetime		Auger lifetime
			Single-particle	Ensemble	Ensemble
Spheroid 1	1100 ± 294 nm ³	~34%	–	–	0.6 ns
Spheroid 2	2800 ± 706 nm ³	~55%	~56%	3.7 ns	3.2 ns
Spheroid 3	9000 ± 1860 nm ³	~75%	~78%	7.5 ns	6.3 ns
Rod 1	3000 ± 1131 nm ³	~53%	~70%	–	2.27 ns
Rod 2	4600 ± 1635 nm ³	~80%	~75%	4.18 ns	4.0 ns

The time window of biexciton lifetime was shown in Additional file 1: Fig. S11 and Fig. S12

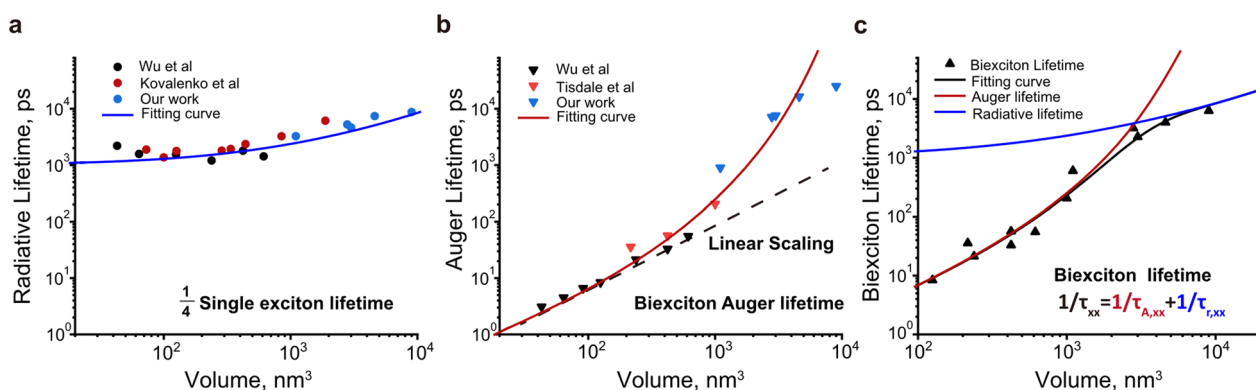


Fig. 4 Analysis of biexciton lifetime from CsPbBr₃ nanocrystals. **a** Size dependence of biexciton radiative lifetime, defined as one quarter of single exciton lifetime [53], and its fitting (blue line) by $\tau_X = \tau_{X0} + aV^\alpha$. The fitting parameters take $\tau_{X0} = 4000$ ps, $a = 55$, and $\alpha = 0.68$. **b** Size dependence of biexciton Auger lifetime and its fitting (red line) by $\tau_{Auger} = bV^\beta e^{(\frac{V}{V_0})^\gamma}$. The fitting parameters take $b = 0.05$ and $V_0 = 450$ nm³ under the theoretical values of $\beta = 1$ (from reference [14]) and $\gamma = \frac{2}{3}$. **c** Size dependence of biexciton lifetime and its fitting (black line) by $\tau_{XX} = \frac{\tau_{r,XX} \times \tau_{Auger}}{\tau_{r,XX} + \tau_{Auger}}$

agreement with experimental data (dots). On the other hand, the Auger recombination lifetime with volume can be simulated using $\tau_{\text{Auger}} = bV^\beta e^{\left(\frac{V}{V_0}\right)^\gamma}$ (b , β , V_0 , and γ are fitting parameters), where V and τ_{Auger} take the units of nm^3 and ps. Considering nonlocal effects in large nanocrystals, the model leads to $V_0 = \frac{4\pi}{3} \left(\frac{\lambda_X}{\pi}\right)^3 \approx 370 \text{ nm}^3$ and $\gamma = \frac{2}{3}$ (see theory part in Additional file 1: Material S1). When the volume takes about 1000 nm^3 ($\sim 2V_0$), the relationship between τ_{Auger} and V changes from linear to exponential, corresponding to a transition from strong confinement to weak confinement. Combining $\tau_{r,XX}$ and τ_{Auger} , we can also fit the biexciton lifetime using $\tau_{XX} = \frac{\tau_{r,XX} \times \tau_{\text{Auger}}}{\tau_{r,XX} + \tau_{\text{Auger}}}$ (see Fig. 4c). The Auger recombination dominates biexciton dynamics in small nanocrystals, while radiative recombination plays a critical role in large nanocrystals, where nonlocal effects make the Auger recombination negligible.

In conclusion, we discovered nonlocal effects of biexciton emission in CsPbBr_3 nanocrystals by comparing our spectroscopic results of large nanocrystals with previously reported small nanocrystals. Such a nonlocal effect can be illustrated by considering the influence of nonlocal effects on Auger recombination. With volume increasing, the Auger recombination rate of large CsPbBr_3 nanocrystals can be greatly reduced to achieve high biexciton efficiency up to 80%. The discovered nonlocal effects in large nanocrystals not only provide a guideline to fabricate advanced quantum emitters with efficient biexciton (multiple exciton) emission, but also create new opportunities to explore semiconductor nanocrystals beyond strong quantum confinement.

4 Methods

4.1 Materials

Lead (II) bromide (PbBr_2 , >99.99%, Alfa Aesar), Cesium bromide (CsBr , >99.99%, Alfa Aesar), Lead (II) oxide (PbO , >99.999%, Aladdin), Cesium carbonate (Cs_2CO_3 , >99.99%, MREDA), Phenacyl bromide ($\text{C}_6\text{H}_5\text{COCH}_2\text{Br}$, >99%, Amethyst Chemicals), 1-octadecene (ODE, >90%, Alfa Aesar), Oleic acid (>90%, Aladdin), Octylamine (>90%, Aladdin), Hexylamine (>90%, Aladdin), n-tetradecylamine (>99%, Aladdin), Dimethyl sulfoxide (DMSO, >99.99%, Aladdin), Isopropanol (>99.99%, Beijing TongGuang Fine Chemicals), Hexane (>99.99%, Beijing TongGuang Fine Chemicals) and Toluene (>99.99%, Beijing TongGuang Fine Chemicals) were used.

4.2 Synthesis of large CsPbBr_3 nano-spheroids

In a typical synthesis, the precursor solution of Cs-oleate was prepared by dissolving 1.2 mmol (390.8 mg) of Cs_2CO_3 into a mixture of 18 mL of 1-octadecene (ODE)

and 2 mL of oleic acid in a three-neck round-bottom flask. The reaction mixture was degassed with nitrogen for 1 h at 120°C , and then kept at 80°C for further use. The Pb precursor solution was prepared by dissolving 0.2 mmol of PbO (44.6 mg), 0.6 mmol of phenacyl bromide (119.4 mg) into a mixture of 1 mL of oleic acid, and 5 mL of ODE in a three-neck round-bottom flask. The precursor solution was degassed at 120°C for 1 h and then increased to 220°C and a fixed amount of amine was injected (n-tetradecylamine is used for Spheroid 1, oleylamine is used for Spheroid 2 and Spheroid 3). The solution turned to yellow around 15 min. After that, 0.5 mL of Cs-oleate precursor solution was swiftly injected into the yellow solution at different temperatures and annealed 30 min for obtaining different size nanocrystals (reaction temperature for Spheroid 1, Spheroid 2 and Spheroid 3 are 200°C , 220°C and 240°C respectively). Crude solution was collected with ice-quenching. 6 mL methyl acetate was added to the 1 mL crude solution and then centrifuged at 8000 rpm for 5 min. Finally, the nanocrystals were precipitated and redispersed in hexane.

4.3 Synthesis of CsPbBr_3 nanorods

A mixture of 0.2 mmol CsBr and 0.2 mmol PbBr_2 was dissolved in 1 mL of DMSO with 120 μL of oleylamine or 60 μL of octylamine and 0.5 mL of oleic acid to form a precursor solution. The sample of Rod 1 was fabricated using octylamine as ligands, while the sample of Rod 2 was fabricated using oleylamine. 1 mL of precursor solution was dropped into 8 mL isopropanol with vigorous stirring. The obtained solution was precipitated by the centrifugation at 6000 rpm for 5 min. The precipitates can be redissolved into 3 mL toluene or hexane to form colloidal nanocrystals solutions.

4.4 Sample preparations for spectroscopic measurements

Colloidal solutions with ~ 0.1 optical density at exciton absorption peak for UV-vis optical absorption and PL spectra. The samples for transient PL spectra were fabricated by transferring a droplet ($\sim 10 \mu\text{L}$) of the colloidal nanocrystal solutions mentioned above to a clean cover slip (micro-liquid films). The samples for single particle spectra were prepared by diluting the solution of the nanocrystals in a polymethyl methacrylate (2.5% by weight in toluene) solution, and spin-casting (5000 rpm, 60 s) the solution on a clean cover slip.

4.5 Morphology and structure characterizations

TEM and HRTEM images were collected using Tecnai G2 F30 S-TWIN transmission electron microscope.

XRD patterns were recorded using a Rigaku SmartLab SE X-ray diffractometer equipped with a Cu K α -radiation source (wavelength of 1.5405 Å).

4.6 Characterizations of the optical properties of solutions

For conventional spectra experiments, UV-vis optical absorption spectra were collected on a UV-6100 UV-vis spectrophotometer (Shanghai Mapada Instruments, China). Steady-state PL spectra were measured using a F-380 fluorescence spectrometer. The absolute PL QY of solutions were determined using a fluorescence spectrometer (calibrated multichannel spectrometer, PMA12) with an integrated sphere (C9920-02, Hamamatsu Photonics, Japan).

4.7 Time-resolved PL spectra measurements

An inverted fluorescence microscope (Olympus IX 83) equipped with a 60 \times oil immersion objective (N.A.=1.49) and suitable spectral filters was used to collect optical spectra of micro-liquid films and single particle. The laser spot is about 400 μm^2 . To measure the transient PL spectra of micro-liquid films and single particle, a 405 nm pump wave laser (PicoQuant) with 1 MHz repetition and ~ 50 ps pulse width was used as the excitation light source and the photoluminescence signal was recorded by a single-photon counting system (a Micro Photon Devices MPD-050-CTD-FC photon detectors with 165 ps resolution and PicoQuant PicoHarp 300 TCSPC module). Photoluminescence intensity traces of single particle was collected with the same single-photon counting system mentioned above in a time-tagged time-resolved (TTTR) mode. Second-order photon intensity correlation measurements were performed with the same system and module with a Hanbury-Brown and Twiss (HBT) experiment set-up comprised of a 50/50 beam splitter and two single-photon detectors.

4.8 Model of emission saturation for biexciton quantum yield calculation.

Calculation of biexciton quantum yield from the PL saturation curve is adapted from the methods in previous work [34]. The photon number absorbed per dot per excitation pulse ($\langle N \rangle$) is assumed to follow the Poisson distribution, the probability of finding a QD in m -exciton state is $P(m, \langle N \rangle) = \langle N \rangle^m e^{-\langle N \rangle} / m!$. At a given pulse, the total PL intensity can model as:

$$I = \sum_{m=1}^{\infty} [\sum_m^{\infty} P(m, \langle N \rangle)] Q_{mx} \quad (1)$$

For multi-exciton emission, the m -excitons quantum yield $Q_{mx} = k_{r,mx} / (k_{r,mx} + k_{nr,mx})$, scaling of the

multi-exciton radiative and non-radiative rates are $k_{r,mx} = m^2 k_{r,x}$ and $k_{nr,mx} = m^2 (m-1) k_{nr,x}$. $k_{r,x}$ and $k_{nr,x}$ are the scaling of the single-exciton radiative and non-radiative rates. Therefore, the total emission intensity curve (I) is essential a function of Q_{2x} and $\langle N \rangle$. Fitting the total emission intensity curve, we can obtain the biexciton quantum yield $Q_{2x} = Q_{Y_{xx}}$.

For single-exciton-only PL intensity, the single exciton emission saturates following the equation:

$$\begin{aligned} I_x &= \sum_{m=1}^{\infty} P(m, \langle N \rangle) Q_x = Q_x (1 - P(0, \langle N \rangle)) \\ &= Q_x (1 - e^{-\langle N \rangle}) = Q_x (1 - e^{-C\mu}) \end{aligned} \quad (2)$$

where $P(m, \langle N \rangle)$ is a Poisson distribution function, Q_x is the single-exciton quantum yield, C is the scaling factor depending on the absorption cross section, μ is the excitation intensity. Therefore, C and $\langle N \rangle$ can be determined by fitting the single-exciton-only PL curve with the function above.

Supplementary Information

The online version contains supplementary material available at <https://doi.org/10.1186/s43593-023-00045-3>.

Additional file 1: Figure S1. TEM images of CsPbBr₃ nanocrystals and their size distributions. **Figure S2.** Powder X-ray diffractions patterns. **Figure S3.** PL and UV-vis absorption spectra. **Figure S4.** Exciton lifetime analysis. **Figure S5.** Single particle blinking behaviors of samples. **Figure S6.** Single particle transient PL spectra of Spheroid 3. **Figure S7.** Ensemble biexciton lifetime analysis. **Figure S8.** $Q_{Y_{xx}}$ obtained from single particle measurements. **Figure S9.** $Q_{Y_{xx}}$ obtained from ensemble samples. **Figure S10.** Transient PL spectra of single Spheroid 2 and Rod 2. **Figure S11.** The time window of biexciton decay for ensemble samples. **Figure S12.** The time window of biexciton decay for single particle samples.

Acknowledgements

This work was by supported by Beijing Natural Science Foundation (Z210018, H. Z.), and National Natural Science Foundation of China (12074037, Y. Z.). We thank Experimental Center of Advanced Materials of Beijing Institute of Technology for technical assistance.

Author contributions

HZ conceived the project. YZ, HQ, and HZ supervised the project. PH and SS fabricated the materials and conduct the characterizations. PH, HL, HQ, and HZ carried out the spectroscopic measurements and performed the analysis. YZ proposed the theoretical model. PH, YZ, HQ, and HZ wrote the manuscript with the contribution from all the authors. All authors read and approved the final manuscript.

Data availability

The datasets used and/or analyzed during the current study are available from the corresponding author on reasonable request.

Declarations

Competing interests

The authors declare no competing financial interests.

Received: 3 March 2023 Revised: 6 April 2023 Accepted: 15 April 2023
Published online: 22 May 2023

References

- A.P. Alivisatos, Semiconductor clusters, nanocrystals, and quantum dots. *Science* **271**, 933–937 (1996)
- G.D. Scholes, G. Rumbles, Excitons in nanoscale systems. *Nat. Mater.* **5**, 683–696 (2006)
- A.L. Efros, L.E. Brus, Nanocrystal quantum dots: from discovery to modern development. *ACS Nano* **15**, 6192–6210 (2021)
- F.P. García de Arquer et al., Semiconductor quantum dots: technological progress and future challenges. *Science* **373**, 8541 (2021)
- M. Jansen, W.A. Tisdale, V. Wood, Nanocrystal phononics. *Nat. Mater.* **22**, 161–169 (2023)
- M. Pelton et al., Efficient source of single photons: a single quantum dot in a micropost microcavity. *Phys. Rev. Lett.* **89**, 233602 (2002)
- P. Senellart, G. Solomon, A. White, High-performance semiconductor quantum-dot single-photon sources. *Nat. Nanotechnol.* **12**, 1026–1039 (2017)
- H. Wang et al., Towards optimal single-photon sources from polarized microcavities. *Nat. Photonics* **13**, 770–775 (2019)
- C.L. Salter et al., An entangled-light-emitting diode. *Nature* **465**, 594–597 (2010)
- M. Müller, S. Bounouar, K.D. Jöns, M. Glässl, P. Michler, On-demand generation of indistinguishable polarization-entangled photon pairs. *Nat. Photonics* **8**, 224–228 (2014)
- H. Wang et al., On-demand semiconductor source of entangled photons which simultaneously has high fidelity, efficiency, and indistinguishability. *Phys. Rev. Lett.* **122**, 113602 (2019)
- R.M. Stevenson et al., A semiconductor source of triggered entangled photon pairs. *Nature* **439**, 179–182 (2006)
- J.-W. Pan et al., Multiphoton entanglement and interferometry. *Rev. Mod. Phys.* **84**, 777–838 (2012)
- C.-Y. Lu, J.-W. Pan, Quantum-dot single-photon sources for the quantum internet. *Nat. Nanotechnol.* **16**, 1294–1296 (2021)
- F. Basso Basset et al., Quantum key distribution with entangled photons generated on demand by a quantum dot. *Sci. Adv.* **7**, 6379 (2021)
- C. Schimpf et al., Quantum dots as potential sources of strongly entangled photons: perspectives and challenges for applications in quantum networks. *Appl. Phys. Lett.* **118**, 100502 (2021)
- J.M. Pietryga et al., Spectroscopic and device aspects of nanocrystal quantum dots. *Chem. Rev.* **116**, 10513–10622 (2016)
- F. Fan et al., Continuous-wave lasing in colloidal quantum dot solids enabled by facet-selective epitaxy. *Nature* **544**, 75–79 (2017)
- H. Utzat et al., Coherent single-photon emission from colloidal lead halide perovskite quantum dots. *Science* **363**, 1068–1072 (2019)
- Y.-S. Park, J. Roh, B.T. Diroll, R.D. Schaller, V.I. Klimov, Colloidal quantum dot lasers. *Nat. Rev. Mater.* **6**, 382–401 (2021)
- K.E. Shulenberger et al., Multiexciton lifetimes reveal triexciton emission pathway in CdSe nanocrystals. *Nano Lett.* **18**, 5153–5158 (2018)
- P. Tyagi, P. Kambhampati, Observing strongly confined multiexcitons in bulk-like CsPbBr₃ nanocrystals. *J. Chem. Phys.* **134**, 094706 (2023)
- T.B. Hoang, G.M. Akselrod, M.H. Mikkelsen, Ultrafast room-temperature single photon emission from quantum dots coupled to plasmonic nanocavities. *Nano Lett.* **16**, 270–275 (2016)
- C.R. Kagan, L.C. Bassett, C.B. Murray, S.M. Thompson, Colloidal quantum dots as platforms for quantum information science. *Chem. Rev.* **121**, 3186–3233 (2021)
- Y.-S. Park, S. Guo, N.S. Makarov, V.I. Klimov, Room temperature single-photon emission from individual perovskite quantum dots. *ACS Nano* **9**, 10386–10393 (2015)
- F. Hu et al., Superior optical properties of perovskite nanocrystals as single photon emitters. *ACS Nano* **9**, 12410–12416 (2015)
- X. Lin et al., Electrically-driven single-photon sources based on colloidal quantum dots with near-optimal antibunching at room temperature. *Nat. Commun.* **8**, 1132 (2017)
- S. Morozov et al., Electrical control of single-photon emission in highly charged individual colloidal quantum dots. *Sci. Adv.* **6**, eabb1821 (2020)
- V.I. Klimov et al., Optical gain and stimulated emission in nanocrystal quantum dots. *Science* **290**, 314–317 (2000)
- V.I. Klimov, J.A. McGuire, R.D. Schaller, V.I. Rupasov, Scaling of multiexciton lifetimes in semiconductor nanocrystals. *Phys. Rev. B* **77**, 195324 (2008)
- H. Igarashi, M. Yamauchi, S. Masuo, Correlation between single-photon emission and size of cesium lead bromide perovskite nanocrystals. *J. Phys. Chem. Lett.* **14**, 2441–2447 (2023)
- C. Melnychuk, P. Guyot-Sionnest, Multicarrier dynamics in quantum dots. *Chem. Rev.* **121**, 2325–2372 (2021)
- J.R. Lakowicz, *Principles of fluorescence spectroscopy* (Springer, Boston, 2006)
- Y.S. Park et al., Near-unity quantum yields of biexciton emission from CdSe/CdS nanocrystals measured using single-particle spectroscopy. *Phys. Rev. Lett.* **106**, 187401 (2011)
- F. García-Santamaría et al., Breakdown of volume scaling in Auger recombination in CdSe/CdS heteronanocrystals: the role of the core–shell interface. *Nano Lett.* **11**, 687–693 (2011)
- Y. Louyer et al., Efficient biexciton emission in elongated CdSe/ZnS nanocrystals. *Nano Lett.* **11**, 4370–4375 (2011)
- M. Nasilowski, P. Spinicelli, G. Patriarche, B. Dubertret, Gradient CdSe/CdS quantum dots with room temperature biexciton unity quantum yield. *Nano Lett.* **15**, 3953–3958 (2015)
- J.D. Jackson, Classical electrodynamics. *Am. J. Phys.* **67**, 841–842 (1999)
- S. Stobbe et al., Spontaneous emission from large quantum dots in nanostructures: exciton-photon interaction beyond the dipole approximation. *Phys. Rev. B* **86**, 085304 (2012)
- C. Qian et al., Nonlocal exciton-photon interactions in hybrid high-q beam nanocavities with encapsulated MoS₂ monolayers. *Phys. Rev. Lett.* **128**, 237403 (2022)
- F.J. García de Abajo, Nonlocal effects in the plasmons of strongly interacting nanoparticles, dimers, and waveguides. *J. Phys. Chem. C* **112**, 17983–17987 (2008)
- J. Kang, L.-W. Wang, High defect tolerance in lead halide perovskite CsPbBr₃. *J. Phys. Chem. Lett.* **8**, 489–493 (2017)
- J.M. Richter et al., Enhancing photoluminescence yields in lead halide perovskites by photon recycling and light out-coupling. *Nat. Commun.* **7**, 13941 (2016)
- X. Zhang, J.-X. Shen, C.G. Van de Walle, First-principles simulation of carrier recombination mechanisms in halide perovskites. *Adv. Energy Mater.* **10**, 1902830 (2020)
- S. Bera, R.K. Behera, N. Pradhan, A-halo ketone for polyhedral perovskite nanocrystals: evolutions, shape conversions, ligand chemistry, and self-assembly. *J. Am. Chem. Soc.* **142**, 20865–20874 (2020)
- F. Zhang et al., Brightly luminescent and color-tunable colloidal CH₃NH₃PbX₃ (X = Br, I, Cl) quantum dots: potential alternatives for display technology. *ACS Nano* **9**, 4533–4542 (2015)
- G. Mannino et al., Temperature-dependent optical band gap in CsPbBr₃, MAPbBr₃, and FAPbBr₃ single crystals. *J. Phys. Chem. Lett.* **11**, 2490–2496 (2020)
- G. Nair, J. Zhao, M.G. Bawendi, Biexciton quantum yield of single semiconductor nanocrystals from photon statistics. *Nano Lett.* **11**, 1136–1140 (2011)
- N.S. Makarov et al., Spectral and dynamical properties of single excitons, biexcitons, and trions in cesium-lead-halide perovskite quantum dots. *Nano Lett.* **16**, 2349–2362 (2016)
- F. Krieg et al., Monodisperse long-chain sulfobetaine-capped CsPbBr₃ nanocrystals and their superfluorescent assemblies. *ACS Cent. Sci.* **7**, 135–144 (2021)
- M.N. Ashner et al., Size-dependent biexciton spectrum in CsPbBr₃ perovskite nanocrystals. *ACS Energy Lett.* **4**, 2639–2645 (2019)
- Y. Li et al., Biexciton Auger recombination in mono-dispersed, quantum-confined CsPbBr₃ perovskite nanocrystals obeys universal volume-scaling. *Nano Res.* **12**, 619–623 (2019)
- V.I. Klimov, Multicarrier interactions in semiconductor nanocrystals in relation to the phenomena of Auger recombination and carrier multiplication. *Annu. Rev. Condens. Matter Phys.* **5**, 285–316 (2014)